IEEE
THE INSTITUTE OF ELECTRICAL AND ELECTRONICS ENGINEERS INC.

SIGNAL PROCESSING
ALGORITHMS, ARCHITECTURES, ARRANGEMENTS, AND APPLICATIONS
SPA 2015
September 23-25th, 2015, Poznań, POLAND

A centerline-based algorithm for estimation of blood vessels radii from 3D raster images

Jacek Blumenfeld, Marek Kocinski, Andrzej Materka
Institute of Electronics
Lodz University of Technology
Lodz, Poland
jacek.blumenfeld@dokt.p.lodz.pl

***Abstract*—Two approaches to Hessian-based estimation of tubular blood-vessel radius from 3D raster images are compared. In the proposed approach, binary skeleton is found for each tubular vessel-tree branch by thresholding the Hessian-derived vesselness image. Coordinates of the binary skeleton are approximated with smooth 3D spline functions. Their derivatives with respect to arc length give local tangent vectors, and thus planes normal to the vessel centerline. A proposed image intensity profile model is then least-squares fitted to the vessel cross-section by those planes, at each skeleton point. The circular vessel local radius is one of the model parameters. In the reference method, the vessel centerline direction is defined by the local Hessian eigenvector corresponding to the smallest eigenvalue. The radius is estimated using a square root of the vessel cross-section area (as obtained by an adaptive thresholding), divided by π. The impact of Frangi Hessian filter parameters and scale selection on the methods' performance is examined. Higher accuracy, precision and robustness to image noise and artifacts is demonstrated for the proposed method. Example of the method suitability for modeling of brain vasculature magnetic resonance images is also presented in this paper.**

Keywords-3D vascularity image analysis, vessel tree modeling, radius-centerline representation

I. INTRODUCTION

Mathematical modeling of the human vascular system is one of the important tasks in biomedical engineering. The models provide quantitative information for vessels shape, allow simulation of blood flow and tissue perfusion, and are essential for personalized diagnosis or surgery. The basis for this modeling are three-dimensional images – magnetic resonance angiography (MRA) or computed tomography (CT) mainly.

The human vessel trees have a form of connected branches of different diameters. To a first approximation their cross-sections are close to circular and the diameter can be considered large (tens of mm for some arteries), medium (one or few mm) and small (tens of micrometers for capillaries) [1]. The best-resolution contemporary whole-body MR scanners provide good quality images with the voxel edge of about 0.5 mm. As a consequence, the small-diameter branches (thinner than the voxel edge) cannot be modelled as pipes of defined geometry, since a number of such vessels may pass through a voxel. A network of such thin branches may contribute to the texture of corresponding image region, and quantitative texture analysis can be used to characterize them for medical diagnosis [2]. Therefore, to build a complete model of the human vasculature, one has to combine different approaches, best describing regions filled with branches of different diameter and topology [3,4]. This paper is aimed at development of an automated method of geometric modeling of relatively thick vascular branches, whose diameter is larger than the length of voxel edge.

In general, there are two approaches to surface modeling of blood vessel branches. One is based on image segmentation, e.g. with the use of level sets and marching cubes [5]. It is computationally time consuming, moreover it is difficult to use it for automated model building. The other, considered in this paper, is based on tracking the vessels centerline and on modeling their cross-sections afterwards, as reviewed in [6] and recently expanded in [7]. The high accuracy and robustness to noise and artifacts of the proposed vessel modeling algorithm is demonstrated with the use of computer-simulated and real-world brain-vasculature MR images. Although the circular cross-section geometry branches are considered, the method is applicable to other shapes, e.g. elliptical and even triangular as in the case of the *superior sagittal sinus* vein.

II. MATERIALS AND METHODS

A. Materials

To evaluate accuracy of the radius estimation algorithm and the effects of noise and artifacts, a set of digital-phantoms – computer-synthesized isotropic-voxel 3D test images – has been created: straight tubes with random orientation and different diameter (1.0, 1.5, 2.5) and a helical shaped tubes with variable radius. The straight tube vessel models had a fixed length of 80a, where a is the voxel edge length. They were placed inside a 100x100x100 voxel cube at randomly selected polar and azimuthal angles, respectively θ and φ [8]. The synthesized image voxel intensity was proportional to the volume of (partial) intersection of a voxel with the tube model, scaled to the range [0,125] [2].

To account for image noise, pseudo-random numbers of Gaussian probability distribution were added to the voxel intensities of the tube image, with zero mean and selected

This work was supported by the Polish National Research Centre under Grant No. 2013/08/M/ST7/00943.

standard deviation of 0, 10, 20 or 30. Three kinds of image artifacts were simulated – an intensity jump of 30, intensity linear ramp (from 200 to 300) and linearly varying contrast (from 0.7 to 1.3). The intensity of resulting images took its values in the range [0,650]. Example images of this type are illustrated in Fig. 1.

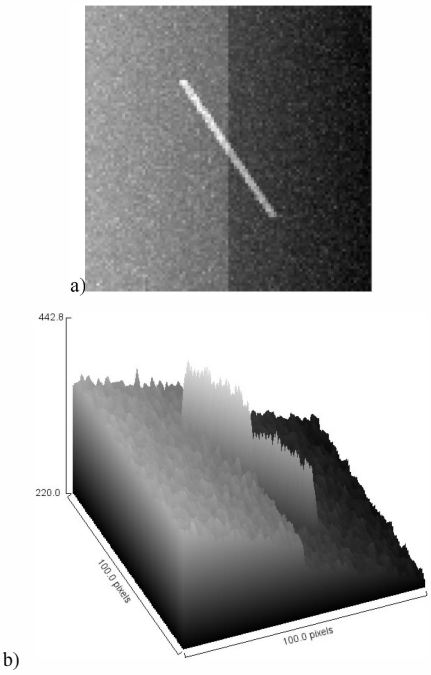

Figure 1. Synthesized image of unity-radius tubular object at θ=54.7°and φ=62.0°, with superimposed intensity jump and linear variation (noise standard deviation = 20): a) maximum intensity projection (MIP) on 0*yz* plane, b) surface plot of the maximum intensity projection.

Surface that encapsulates a helical shaped model is generated based on helix parametric equation. Radius of a tube, corresponding to surface of a vessel, varies along the center according to (1) where x_O, y_O, z_O are the helix center co-ordinates, R_L is the loop radius, r is the initial tube radius, and c is a constant. Vertical separation of the loops is 6π. Example synthesized noisy image of a helical object is shown in Fig. 2.

$$\begin{aligned} x &= x_O + [R_L + r(1+cp)\cos(q)]\cos(p) \\ y &= y_O + [R_L + r(1+cp)\cos(q)]\sin(p) \\ z &= z_O + r(1+cp)\sin(q) + 2p \\ q &\in [0,2\pi], \quad p \in [0,3\pi] \end{aligned} \tag{1}$$

The QSM brain MR images were measured for seven healthy subjects (approved by the ethical committee of Friedrich Schiller University in Jena, Germany) with a flow compensated 3D single-echo gradient-echo sequence (TE/TR/FA/BW = 10.5ms/17ms/8°/140Hz/px, voxel size = (0.4×0.4×0.4)mm^3 on a 7 T MRI system. The scans were carried out with three different orientations of the subject's head with respect to the magnetic field to implement the COSMOS approach [9], further co-registered. Phase aliasing was resolved by 3D phase unwrapping and background phase contributions were eliminated with the SHARP technique [10]. A MIP visualization of a fragment of one of the QSM images of this study is presented in Fig. 3.

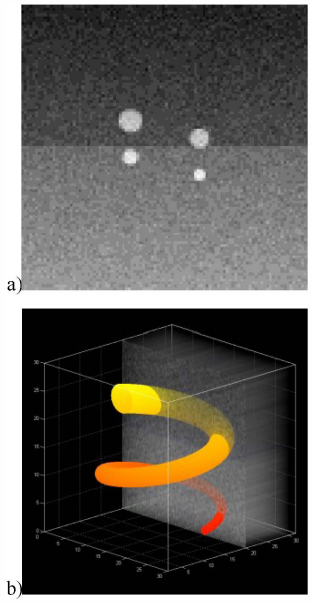

Figure 2. Synthesized image of a helix (r=1, c=0.2, noise standard deviation equals 20): a) 50th cross-section, b) 3D model of the tube.

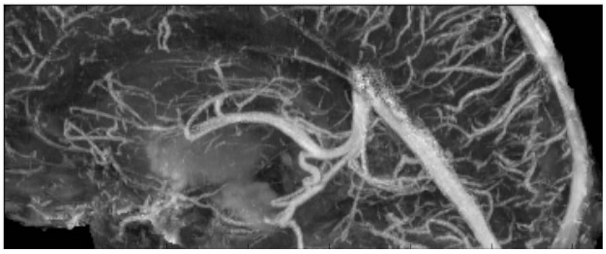

Figure 3. An example MIP of the brain QSM image.

B. *Methods*

In the first step of our algorithm, binary centerlines of tubular object regions are automatically computed. For this purpose, a multi-scale Hessian-based vessel filter [11] is applied to the image. In effect, tubular shapes in images are enhanced through Hessian eigenvalue analysis. In our method the centerlines are initialized as binary skeletons of thresholded vesselness images. To account for varying vessel diameter along its centerline, a number of filtered images are computed, each for different value of σ, the underlying Gaussian kernel [12]. The scale coefficient σ has to be matched to the diameter of tubular objects. Accordingly, the thin vessel regions are enhanced by a kernel with small-scale and regions of thicker vessels by kernels with higher scale values. The maximum of different-σ filtered intensity images found for each voxel is taken as the vesselness filter output (VEF).

It has been observed [13] that the vesselness filter should be adjusted to the tubular objects structure by weighting the different-σ responses prior to finding the maximum across the scales. The simplest weighting method suggested in [11,12] relies on multiplying the Hessian matrix by a scale-dependent coefficient σ^γ where γ is a constant. We have carried out a number of experiments in which images of single tubular objects as well as of separate objects with parallel centerlines

closely positioned to each other (not shown in this paper) were filtered using different values of γ. It was found that γ=2 (recommended in the literature [e.g. 12,13,14] as providing equal filter responses for different scales) leads to vessel blurring with resulting displacement and disappearance of some skeleton lines. Choosing 1≤γ≤1.5 enhances the small-scale responses giving representative skeletons as will be shown later.

Hessian-derived vesselness images are thresholded and then skeletons are found of the resulting binary images with the use of an ITK-based, home-compiled vKnife software. Next, in the second step of the algorithm, all *n*-furcations of the binary skeleton are detected and the skeleton is split into M non-furcating segments. Each of those segments is supposed to represent a part of a tubular object (a branch of the blood vessel system). Sufficiently long skeletal objects are preserved, containing more than few voxels each, to maintain representation of elongated tubular structures.

Consider an *m*-th branch $\{v_m\}=\{v_{m1}, v_{m2},..., v_{mK_m}\}$ of the skeleton, m=1,2,…M, where K_m is the number of voxels in it. To simplify notation, one can neglect the branch index $\{v\}=\{v_m\}$, $K=K_m$, and write

$$\{v\}=\{v_1, v_2,..., v_K\} \tag{2}$$

where $v_k=(x_k, y_k, z_k)$, k=1,2,…K, denote coordinates of the consecutive voxels of the considered skeleton branch. For each point, an arc length l_k of the branch (since its beginning at k=1) can be approximated as

$$l_k=\sum_{k=2}^{K} l_{k-1}+\sqrt{(x_k-x_{k-1})^2+(y_k-y_{k-1})^2+(z_k-z_{k-1})^2} \tag{3}$$

where l_1=0. In the third step of the algorithm, the coordinates of the binary skeleton segment of each tube are approximated by continuous functions $f_x(l), f_y(l), f_z(l)$. These functions are found using spline approximation to the respective three sets $\{x_k, l_k\}$, $\{y_k, l_k\}$, $\{z_k, l_k\}$. In the fourth step, the derivatives of these functions with respect to the parameter l

$$t_x=\frac{df_x}{dl}, \quad t_y=\frac{df_y}{dl}, \quad t_z=\frac{df_z}{dl} \tag{4}$$

can be computed for each k=1,2,…,K. They approximate components of the tangent vector $t_k=(t_{xk}, t_{yk}, t_{zk})$ to the skeletal line. In the fifth step of the algorithm, a normal (vessel cross-section) plane π_k to the t_k vector is found at each skeletal point of each of the skeleton segments – e.g. through appropriate quaternion [15] calculations. Local orientation of the centerline is used to define the normal plane at each centerline point.

In the sixth step of the proposed algorithm, the image intensity profile function inside the vessel region is used to model the actual image intensity at the distance d from a tube centerline, in N angular directions on this plane (see Fig. 4 for N=8). The following smooth model is used in our study

$$u(d; V_0, \Delta_V, R, w)=V_0+\Delta_V\, erfc\left(\frac{d-R}{w}\right) \tag{5}$$

where *erfc*(.) is the complementary error function and V_0 (intensity of the surrounding tissue), Δ_V (intensity increase inside the vessel, above V_0), w (variable related to the width of the intensity transition from vessel to background), and R (the vessel radius) are the parameters. The parameter w accounts for the extent of object edge blurring and is related to the imaging system point spread function (PSF). One can show that in the case of simulated 3D images where the PSF represents the effect of voxel partial volume, the average value of parameter w (accounting for all possible edge directions with respect to voxel walls) can be set to 0.437. A more detailed description of the derivation of this value, as well as theoretical foundation of the usage of complementary error function for modeling the edge blur is given in [16]. To account for the actual PSF of the imaging system, the value of w in (5) has to be independently identified from a selected edge region.

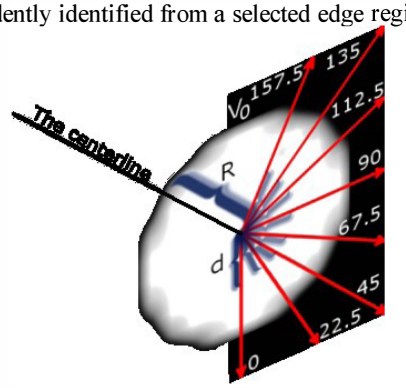

Figure 4. Cross-section profile lines defined on the normal plane (N=8).

In the seventh step of the algorithm, the model (5) is fitted to actual image intensity along the normal-plane profile lines by minimizing the following error function in the (V_0, Δ_V, R) parameter space

$$e(V_0, \Delta_V, R)=\sum_{n=1}^{N}\sum_{i=1}^{Q}[v(d_{ni})-u(d_{ni}; V_0, \Delta_V, R)]^2 \tag{6}$$

where u(.) is given by (5) and Q is the number of points considered along each profile line direction. The image intensity values on the normal plane are obtained via 3D interpolation. The square root of error (6) divided by NQ is the fitting rms error at skeleton point k, denoted by e_N. Similarly, e_Q (a square root of the inner sum in (6) divided by Q) is the rms fitting error for the n-th profile. The least-squares error (6) minimization is done numerically (and can easily be parallelized). The resulting values of local vessel radius R_k at each skeleton point, along with the spline-approximated centerline points are used for tubular object surface modeling.

The performance of the proposed radius estimation algorithm is compared to the one recently presented in [7] where the normalized Hessian eigenvector corresponding to the smallest-magnitude eigenvalue is used to estimate the local centerline direction and then the vessel cross-section by a plane normal to this eigenvector. In the reference method, the radius at centerline point k is estimated by

$$R_k^{ref} = \sqrt{\frac{A_k}{\pi}} \qquad (7)$$

where A_k is the area occupied by the tubular object after thresholding. The threshold value in our project was equal to the average of image intensity in a small neighborhood of the cross-section center and the average intensity of a circle with a radius sufficiently larger than the expected vessel radius.

III. RESULTS

A. Selection of vesselness filter parameters

First, the influence of the normalization parameter γ on the Hessian-based image filter response was investigated. Some of the results are shown in Fig. 5. Each of the three diagrams shows plots of the vesselness filter response [11,12,13,14] to a circular object of fixed radius (R=1.5), with the centerline parallel to the 0z axis, crossing the 0xy plane at x=50, y=50.

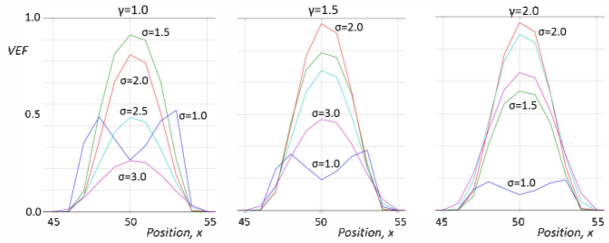

Figure 5. The relative vesselness filter responses to a tube of radius 1.5 for Hessian multiplied by σ^{γ}; γ=1.0 (left), 1.5 (middle), 2.0 (right)

As it is demonstrated in Fig. 5, the relative single-scale responses depend on the value of γ. When selecting the scale σ of the filter, the width of filtered object must be considered. If the width of a tube is much greater than σ, tube's edges are enhanced which may lead to division of the tube region. Then, larger scale filters (giving larger maximum response) should be considered to prevent such region split. For greater values of σ, the tube region is blurred which in a worse case can result in false merging of close objects. Taking into account all of these effects, for straight tube test objects a range of scales was set to [0.5, 4.0] and for the helix datasets the range of σ was [0.5, 2.5]. In both cases, γ=1.5 and the values of σ were changed in steps of 0.5. For the QSM data, the range [1.0,4.0] and step 0.25 were selected for σ, and γ=1.0 was applied to normalize the Hessian matrix. Although in practice, the vesselness filter parameters can be adjusted for images at hand, the issue of optimizing the vesselness filter to obtain faithful centerline representation still needs further research [13]. The errors of the centerline local direction estimation due to image noise slightly increase with reduction of γ, but this effects do not seem to be statistically significant.

B. Radius estimation

Errors in estimation of the centerline orientation angles with the use of the two methods are compared in Fig. 6 for a tube image with R=1.5. The linear intensity ramp with a jump in the middle and Gaussian noise of standard deviation = 10 were included in the tube image used for the angles estimation. Their true values were θ=54.7°and φ=62.0°. One can see that the proposed method ensures high accuracy of angles estimation, with an error less than 1°. For the Hessian-derived angles, the error is much larger. Both, the intensity artefacts and noise have significant effect on the centerline orientation estimated with the use of locally computed Hessian eigenvectors. The error standard deviation for the reference method can be even 20 times larger in the case of noisy images.

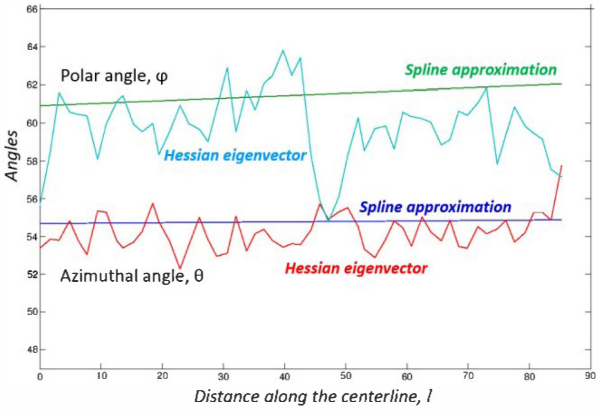

Figure 6. Estimated polar and azimuthal angles of the centerline of a tubular object with R=1.5 (intensity linear ramp, intensity jump in the middle, Gaussian noise of standard deviation = 10).

The errors in measurement of tangent vector orientation make the angle of the vessel cross-section plane different from normal to the centerline. This affects the shape of the tubular object intersection with this plane and causes errors in the vessel radius estimation. A number of experiments were carried out using the synthesized tube images with different artefact and noise to quantify those errors. The results of these experiments are presented in Table I and Table II. Since there is not much difference between effects of brightness and contrast artefacts on the radius estimation errors, the case of images with a linearly varying contrast and the intensity jump is presented in the Tables only. The symbols g0, g10, g20 and g30 refer to Gaussian noise standard deviation, respectively of 0, 10, 20, and 30, compared to [0,650] range of the simulated 3D image intensity.

TABLE I. MEAN VALUE AND STANDARD DEVIATION OF AN ERROR IN ESTIMATING STRAIGHT TUBES RADII BY MEANS OF THE PROPOSED ALGORITHM

R	g0		g10		g20		g30	
	mean	*stdev*	*mean*	*stdev*	*mean*	*stdev*	*mean*	*stdev*
1.0	0.012	0.040	0,016	0,055	-0, 006	0,076	0,002	0, 122
1.5	0.048	0.024	0,045	0,042	0,046	0,067	0,048	0,118
2.5	0.053	0.019	0,053	0,029	0,065	0,056	0,056	0,066

As it can be seen in Table I, the absolute mean value of the error experienced with the proposed algorithm does not exceed the value of 0.1 in any considered case. The error standard deviation increases with the standard deviation of the image intensity noise. Still its values are not larger than a fraction of the voxel edge length; apparently a subvoxel accuracy is achieved with the proposed radius estimator.

TABLE II. MEAN VALUE AND STANDARD DEVIATION OF AN ERROR IN ESTIMATING STRAIGHT TUBES RADII BY MEANS OF THE REFERENCE ALGORITHM

R	g0		g10		g20		g30	
	mean	stdev	mean	stdev	mean	stdev	mean	stdev
1.0	-0,326	0,210	-0,402	0,324	-0,829	0,411	-1,237	0,319
1.5	-0,052	0,041	-0,005	0,039	0,014	0,087	-0,071	0,133
2.5	0,151	0,070	0,224	0,072	0,268	0,082	0,329	0,074

The errors are definitely larger in the case of the reference formula (7), based on Hessian eigenvector centerline orientation and implemented after [7]. It follows from Table II that the magnitude of the mean error is largest for thin tube (R=1.0). This error is comparable to the radius value itself. More detailed inspection (not shown here) indicates that in the region of the image intensity jump the error may exceed the true radius value even a few times. The mean error decreases for a thicker tube (R=1.5) and increases again for R=2.5 which may be related to a systematic error introduced by the threshold selection algorithm.

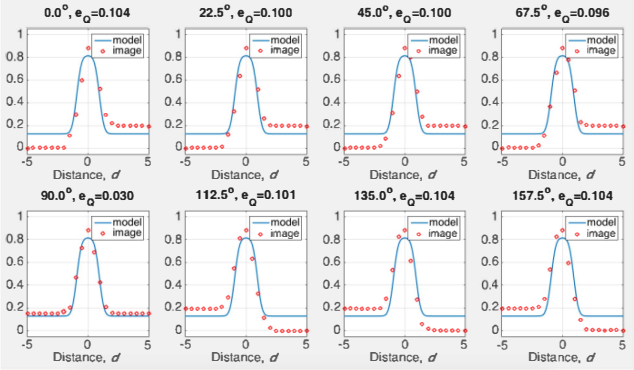

Figure 7. Image model (3) least-squares fitted along N=8 profile lines to the simulated image of R=1.0 tube passing through the intensity jump, w=0.437. The negative values of d correspond to the distance measured from centerline to the object edge in the direction of the tails of the arrows shown in Fig. 4.

Comparison of the tube radius estimation by the two considered methods (Table I and Table II) indicates that the proposed estimator does not depend, in practice, on the intensity and contrast variations, including intensity jumps. This robustness to the image artifacts can be explained by noting that the radius estimation is obtained through fitting the edge blur model (5) to the image values. The fitting is an adaptive process which involves adjustment of three parameters – (V_0, Δ_V, R). In the places of varying intensity (due to its jump or slow variation) the parameters V_0 and Δ_V are adjusted accordingly. The information about the edge location (and thus R) is included in the actual, rather steep, transition between the inside (V_0+Δ_V) and the outside (V_0) intensity of the tubular object. The location of this transition is only slightly affected by those two intensities, and therefore they have little effect of the radius estimation. This is illustrated in Fig. 7 where the tube profiles stay almost independent of the background intensity jump.

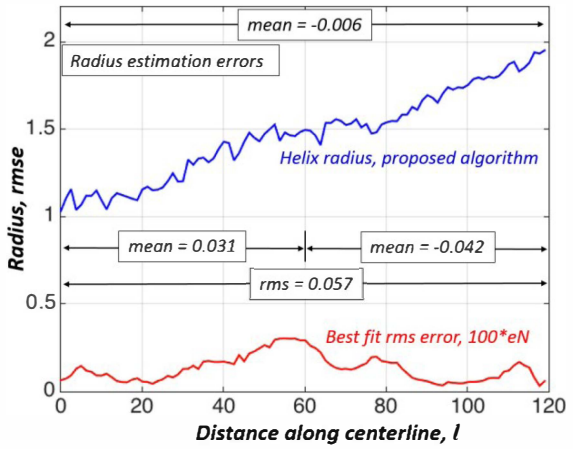

Figure 8. Radius of a helix (r=1, c=0.1, linear intensity with a jump, noiseless image) estimated using the proposed algorithm.

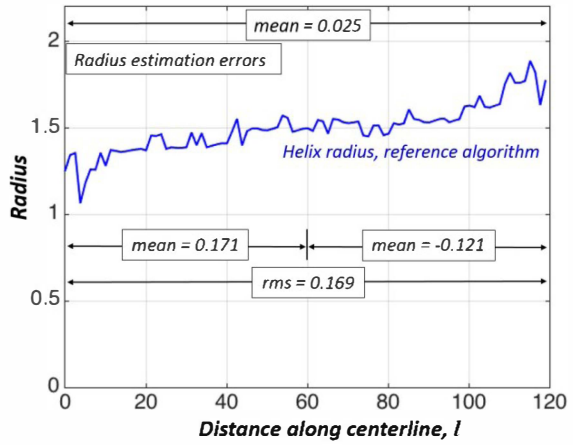

Figure 9. Radius of a helix (r=1, c=0.1, linear intensity with a jump, noiseless image) estimated using the reference algorithm.

The superior accuracy of the proposed algorithm was also confirmed by helical objects radius estimation (Figs. 8 and 9). Again, a subvoxel accuracy is achieved with the proposed algorithm as the true radius changes from 1.0 to 1.9 along the helix centerline. In Fig. 9, showing the performance of the reference method, much larger differences are observed. Again, the image artifacts have significant effect on radius estimated by the reference algorithm, with practically no effect on the proposed method result. The images of a high-curvature helix object (Fig. 2) can also be used to explain the superiority of the proposed technique in terms of accurate approximation of the centerline local direction, compared to the locally computed Hessian eigenvectors. This is illustrated in Fig. 10 where the staircase-like plots of the helix skeleton are shown next to smooth curves representing the tangent vector components computed from spline-approximated functions (4). One can say the knowledge included in the shape of the skeleton 3D curve is utilized in the proposed algorithm to make it more accurate in predicting the tangent vector orientation than the local Hessian eigenvalues.

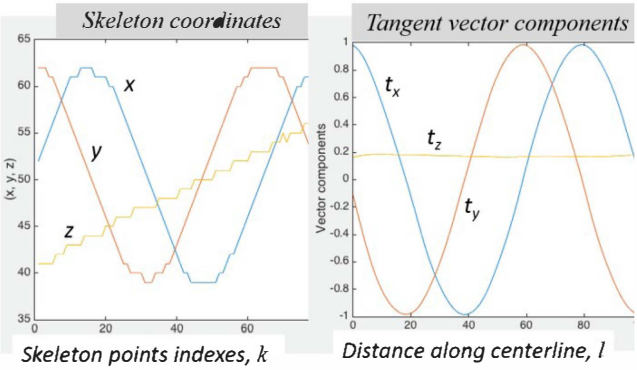

Figure 10. Helix skeleton coordinates (left) and tangent vector components (right) estimated with proposed algorithm [noisy (g30) image with artifacts].

To extract the skeleton of the major vessels visualized in the brain QSM image, thirteen Frangi-vesselness images were computed [11], respectively using σ=1.0,1.25,…,4.0. The Hessian was multiplied by σ^{γ}, γ=1, prior to eigenvalue analysis. The maxima across scales were selected for each voxel to make the vesselness image, thresholded at 8% of the maximum, and skeletonized.

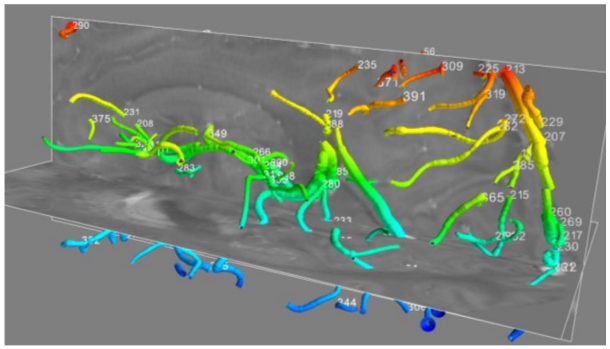

Figure 11. Visual presentation of selected surface-triangulated smoothed tubular branches extracted from the QSM brain image in Fig. 3.

The *R*-centerline data vectors computed for the parsed skeleton branches were used for visual rendering as tubes of triangulated surface (Fig. 11). Smoothed *R*-centerline profiles were used to compute the relevant .stl files. The tubes representing bifurcating branches were joined together as logical union of their slightly extended meshes. Further work is under way to evaluate accuracy of the MRA-derived vessel model using properly designed flow phantoms [17].

IV. Conclusion

A centerline-based method for automated estimation of the radii of tubular blood vessel segments, basing of their raster 3D images was designed. It was validated with the use of simulated 3D images and applied to 7 T QSM brain vasculature volumes. Its robustness to noise and artifacts is achieved through effective tuning of vesselness filters, further strengthened by spline centerline approximation of the binary skeleton – for accurate tangent vector estimation. Least-squares fit of the intensity profiles over normal-plane cross-sections gives reliable radius estimation along centerline. The value of the residual error provides clues on discrepancies from the assumed circular symmetry (active contours can be applied in such cases), and for the presence of bifurcations. The radius-centerline datasets were used for blood vessel branches visualization and modeling for blood flow simulation.

Acknowledgment

The authors thank Doctor Andreas Deistung and Professor Juergen R. Reichenbach for kindly providing the volunteer brain vasculature QSM MR images used in this study.

References

[1] W. Boron, E. Boulpaep, Medical Physiology, 2nd edition, Sounders, 2012, pp. 429-447.

[2] M. Kocinski, A. Klepaczko, A. Materka, M. Chekenya, and A. Lundervold, "3D image texture analysis of simulated and real-world vascular trees", Computer Methods and Programs in Biomedicine, vol. 107, pp. 140-154, 2012.

[3] A. Quarterioni, "Modeling the cardiovascular system – a mathematical adventure: part I", SIAM News, vol. 34(5), pp. 1-3, 2001.

[4] A. Quarterioni, "Modeling the cardiovascular system – a mathematical adventure: part II", SIAM News, vol. 34(6), pp. 1-3 (2001).

[5] Vascular Modeling Toolkit, http://www.vmtk.org, accessed April 2015.

[6] D. Lesage, E.D. Angelini, I. Bloch, and G. Funka-Lea, "A review of 3D vessel lumen segmentation techniques: models, features and extraction schemes", Medical Image Analysis, vol. 13, pp. 819-845, 2009.

[7] F. Yuan, Y. Chi, S. Huang, and J. Liu, "Modeling n-furcated liver vessels from a 3D segmented volume using hole-making and subdivision methods", IEEE Transactions on Biomedical Engineering, vol. 59, pp. 552-561, 2012.

[8] Wikipedia, "Spherical coordinate system", http://en.wikipedia.org/wiki/Spherical_coordinate_system, accessed on April 24, 2015.

[9] T. Liu, P. Spincemaille, L. De Rochefort, B. Kressler, and Y. Wang, "Calculation of susceptibility through multiple orientation sampling (COSMOS): a method for conditioning the inverse problem from measured magnetic field map to susceptibility source image in MRI", Magnetic Resonance in Medicine, vol. 61, pp. 196-204, 2009.

[10] M. Jenkinson, P. Bannister, M. Brady, and S. Smith, "Improved optimization for the robust and accurate linear registration and motion correction of brain images", Neuroimage, vol. 17, pp. 825-841, 2002.

[11] A.F. Frangi, W.J. Niessen, P.J. Nederkoorn, J. Bakker, W.P.T.M. Mali, and M. Viergever, "Quantitative analysis of vascular morphology from 3D MR angiograms: in vitro and in vivo results", Magnetic Resonance in Medicine, vol. 45, pp. 311-322, 2001.

[12] A.F. Frangi, W.J. Niessen, K.L.Vincken, and M.A. Viergever, "Multiscale vessel enhacement filtering", MICCAI'98, Springer LNCS 1496, pp. 130-137.

[13] O.P. Dzyubak and E.L. Ritman, "Automation of Hessian-based tubularity measure response function in 3D biomedical images", International Journal of Biomedical Imaging, vol. 2011, Article ID 920401, 16 pages, doi:10:1155/2011/920401.

[14] T. Lindeberg, "Feature detection with automatic scale selection", Int. Journal of Computer Vision, vol. 30, no. 2, pp. 79-116, 1998.

[15] F. Dunn and I. Parberry, 3D Math Primer for Graphics and Game Development, 2nd ed., CRC Press, 2012.

[16] A. Materka, M. Kocinski, J. Blumenfeld, A. Klepaczko, A. Deistung, B. Serres, J.R. Reichenbach, "Automated modeling of tubular blood vessels presented in 3D MR angiography images", submitted for publication.

[17] A Klepaczko, A Materka, P Szczypinski, M Strzelecki, „Numerical modeling of MR angiography for quantitative validation of image-driven assessment of carotid stenosis", IEEE Transaction Nuclear Science, vol. 62., no. 3, pp. 619-627, 2015.